Mean kinetic energy transport and event classification in a model wind turbine array versus an array of porous disks: Energy budget and octant analysis

Elizabeth H. Camp* and Raúl Bayoán Cal†
Department of Mechanical and Materials Engineering, Portland State University, Portland, Oregon 97201, USA
(Received 9 March 2016; published 1 August 2016)

An array of model rotating wind turbines is compared experimentally to an array of static porous disks in order to quantify the similarities and differences in the mean kinetic energy transport within the wakes produced in these two cases. Stereo particle image velocimetry measurements are done in a wind tunnel bracketing the center turbine in the fourth row of a 4×3 array of model turbines. Equivalent sets of rotors and porous disks are created by matching their respective induction factors. The primary difference in the mean velocity components is found in the spanwise mean velocity component, which is as much as 190% different between the rotor and disk case. Horizontal averages of mean kinetic energy transport terms in the region where rotation is most important show percent differences in the range 3%–41%, which decrease to 1%–6% at streamwise coordinates where rotation is less important. Octant analysis is performed on the most significant term related to vertical mean kinetic energy flux $\overline{u'v'}U$. The average percent difference between corresponding octants is as much as 68% different in the near wake and as much as 17% different in the far wake. Furthermore, octant analysis elucidates the three-dimensional nature of sweeps and ejections in the near wake of the rotor case. Together, these results imply that a stationary porous disk adequately represents the mean kinetic energy transport of a rotor in the far wake where rotation is less important, while significant discrepancies exist at streamwise locations where rotation is a key phenomenon. This comparison has implications in the use of an actuator disk to model the wind turbine rotor in computational simulations specifically for studies where Reynolds stresses, turbulence intensity, or interactions with the atmosphere are of interest.

DOI: 10.1103/PhysRevFluids.1.044404

I. INTRODUCTION

The power production capacity from wind energy continues to increase as new wind turbines and wind turbine arrays are installed worldwide [1]. Wind turbine wakes can persist more than 15 rotor diameters D downstream of wind turbines [2], while the spacing in many operational wind farms is much less than this distance and hence many turbines are influenced by the wake of neighboring turbines. Thus, in a wind farm, the wakes of upstream turbines affect the power production [3,4], dynamic loading [5], and fatigue characteristics [6] of turbines downstream. Wind turbine wakes in wind turbine arrays also interact with the atmospheric boundary layer, which in turn affects the surface heat flux [7] from the earth in the vicinity of the turbines and, in large farms, may influence local micrometerology [8]. Since wind turbine wakes are key in all of these phenomena, from power production to atmospheric influence, it is critical to understand and predict these wakes.

Both experimental measurements and computational fluid dynamics (CFD) work have contributed to the understanding of wind turbine wakes as well as the ability to predict such flows [9].

*betsy.h.camp@gmail.com
†rcal@pdx.edu

Among computational codes based on the Navier-Stokes equations, turbulence models based on the Reynolds averaged Navier-Stokes (RANS) equation as well as large-eddy simulations (LESs) are the current state of the art for flows involving wind turbines and wind farms [10]. In addition to a turbulence model, a model for the wind turbine rotor is needed in CFD simulations. Two such turbine models are the actuator disk (AD) model and the actuator line (AL) model [11]. In computational work, the calculated data are influenced by both the turbulence model and rotor model used to generate it.

Studies have been performed to compare different turbine models used in computational simulations to determine their impact on the resulting computed data. Wu and Porté-Agel [12] compared LESs of two different AD models to a physical wind turbine model in a wind tunnel. Both AD models resulted in flow fields that differed dramatically from one another and from the measured wind tunnel turbine model in the near wake. The mean velocity components of all three cases became quite similar by five rotor diameters downstream, while turbulence intensity and Reynolds shear stress still showed discrepancies until $10D$ and $20D$ downstream, respectively. Martínez-Tossas *et al.* [13] compared LESs of an AD model and AL model with wind tunnel measurements of a model turbine having a rotor with the same airfoil profile. While the mean velocity profiles of the AD and AL models were nearly the same in the near wake, they differed from the wake of the wind tunnel model with the greatest discrepancies occurring directly downstream of the turbine nacelle. Power production estimates of the two turbine computational models differed by less than 1%.

In the wind energy context, it is difficult to create equivalent computational simulations and wind tunnel simulations for comparison [14]. Some of these challenges arise during the calculation of the turbine model parameters to be used in the CFD simulation due to uncertainty in the physical blade profile [15,16]. Such issues have motivated the use of physical experiments to compare the wakes from actuator disk modeled turbines with those from turbines modeled using rotors. Wind tunnel measurements by Aubrun *et al.* [17] performed utilizing hot-wire anemometry compared the physical equivalent of an actuator disk, a stationary porous disk, with a matched turbine model having a three-bladed rotor under two inflow conditions. The mean streamwise velocity and the skewness and kurtosis of the streamwise velocity between the porous disk and rotor display the most significant disparities in the near wake. However, by three diameters downstream, they became nearly the same. Lignarolo *et al.* [18] used stereo particle image velocimetry (PIV) to measure the wake between $0.1D$ and $2.2D$ downstream of a porous disk and matched model wind turbine rotor in a wind tunnel with uniform inflow. The greatest differences in the flow characteristics were found at small downstream distances. However, by $2.2D$ downstream, the axial velocity and all three components of the turbulence intensity were nearly identical. Of the quantities compared, the greatest disparities between rotor and disk cases were in the mean kinetic energy transport at radial coordinates in the vicinity of the turbine model blade tip.

Single wind turbines and turbines at the periphery of wind farms function differently from those positioned within a wind turbine array [3,19]. This has made it necessary to conduct studies on model wind turbine arrays (e.g., [20,21]) to augment knowledge gained from work done on single turbines. Similarly, studies are needed to compare the flow fields from an array of porous disks with an array of model turbines having rotors.

The similarities and differences in the wakes of porous disk modeled turbines and three-bladed model turbines deep within a turbine array are examined via a wind tunnel experiment. The present analysis of the mean kinetic energy budget in both the near and far wakes allows a detailed comparison of terms relevant to power production in wind farms as well as interaction with the fluid above the array. The interaction of turbine wake with the fluid above the turbine array is investigated since energy exchange between the fluid above and within the array accounts for a significant influx of the kinetic energy allowing wake remediation in large wind farms [20–22]. In addition, octant analysis is used to conditionally average the term most relevant to vertical mean kinetic energy flux in order to link the direction of the velocity fluctuations to the vertical entrainment of mean kinetic energy. From octant analysis, inferences can be made so as to contrast the mechanism by which mean kinetic energy is brought into the array from aloft in the two model farms.

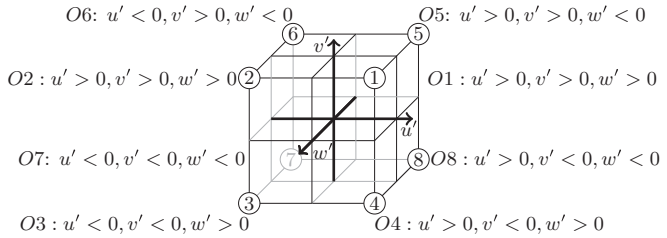

FIG. 1. Relationship between the octant number and the sign of the fluctuations in the x, y, and z directions given by u', v', and w', respectively. Octant labels are given as $O1$–$O8$.

II. THEORY

The equation for the kinetic energy of the mean flow can be found by taking the scalar product of the RANS equation with the mean velocity and contracting free indices to obtain

$$U_j \frac{\partial K}{\partial x_j} = \frac{\partial}{\partial x_j}\left\{-\frac{1}{\rho} P U_i \delta_{ij} - \overline{u_i' u_j'} U_i + 2\nu S_{ij} U_i\right\} + \overline{u_i' u_j'} \frac{\partial U_i}{\partial x_j} - 2\nu S_{ij} S_{ij}, \tag{1}$$

with $U_1 = U, U_2 = V$, and $U_3 = W$ being the streamwise, wall-normal, and spanwise components of the mean velocity, respectively. The corresponding fluctuating components are denoted by lowercase and primes. For example, $u_1' = u'$ indicates the fluctuating component of the streamwise velocity. Time averaging is denoted by an overline on the time-averaged quantities. The advection of mean kinetic energy is expressed as $U_j \partial K/\partial x_j$ in Eq. (1), where K is defined using the relation $K = (1/2) U_i U_i$, with $i = 1$, 2, and 3. The three terms shown in curly braces on the right-hand side of Eq. (1) represent the transport of mean kinetic energy by the pressure gradient, transport of mean kinetic energy by the turbulence itself, and transport due to viscosity, respectively. The production of turbulent kinetic energy (TKE) is represented by $\overline{u_i' u_j'} \partial U_i/\partial x_j$, which acts as a route for energy to be exchanged between the mean flow and the fluctuations. The production term often acts to decrease the kinetic energy of the mean flow while adding energy to the fluctuations. The dissipation of mean kinetic energy directly to internal energy is expressed as $-2\nu S_{ij} S_{ij}$, where the mean strain rate is defined by $S_{ij} = 1/2(\partial U_i/\partial x_j + \partial U_j/\partial x_i)$. Since $S_{ij} S_{ij}$ is always a positive quantity, the dissipation term always acts to remove kinetic energy from the mean flow. Terms expressing the thrust of the turbines have not been included in Eq. (1) since the model turbines are just outside the measurement region.

In order to further investigate the vertical transport of mean kinetic energy, conditional averaging is employed. Quadrant analysis is a method of conditional averaging based on categorizing the sign of the instantaneous fluctuations u' and v' [23]. Octant analysis is an extension of this technique based on categorizing the sign of three instantaneous fluctuations, namely, u', v', and w'. Figure 1 shows the relationship between the octant number and the signs of u', v', and w'. Octants 2 and 6 both represent sweeps since $u' > 0$ and $v' < 0$, although in $O2$, $w' > 0$, whereas in $O6$, $w' < 0$. Similarly, $O4$ ($u' > 0$, $v' < 0$, and $w' > 0$) and $O8$ ($u' > 0$, $v' < 0$, and $w' < 0$) both denote ejections. Outward interactions are represented by $O1$ ($u' > 0$, $v' > 0$, and $w' > 0$) and $O5$ ($u' > 0$, $v' > 0$, and $w' > 0$). Inward interactions are given by $O3$ ($u' < 0$, $v' < 0$, and $w' > 0$) and $O7$ ($u' < 0$, $v' < 0$, and $w' < 0$). Octant analysis has been used to analyze three-dimensional boundary layers such as that near a wing-body junction [24] and a case near a prolate spheroid [25].

Conditionally averaged quantities are denoted by the symbol $\overline{\cdots}$. The conditional average of the kinetic energy flux term is computed via octant analysis by performing

$$\overline{\overset{..}{u'v'U}}_k(x,y) = \frac{U(x,y)}{N} \sum_{n=1}^{N} u_n'(x,y) v_n'(x,y) I_k[u_n'(x,y); v_n'(x,y); w_n'(x,y)], \tag{2}$$

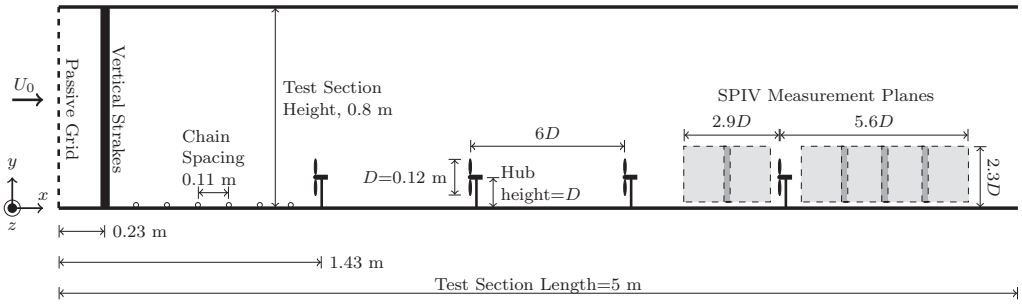

FIG. 2. Side view of tunnel test section with experimental apparatus (for reference only: drawing not to scale).

where k is the octant number (1–8), n is the index of a given sample, N is the total number of samples, x is the streamwise coordinate, and y is the wall-normal coordinate of the measurement location. The step function I_k is defined as

$$I_k[u_n'(x,y);v_n'(x,y);w_n'(x,y)] = \begin{cases} 1 & \text{for } (u_n',v_n',w_n') \text{ in octant } k \\ 0 & \text{otherwise.} \end{cases} \tag{3}$$

The binning of the instantaneous values of the fluctuations illustrates the instantaneous direction of the fluctuations relative to the mean flow. As a result, the conditional average of the vertical transport of mean kinetic energy $\overline{u'v'U}$ in Eq. (2) shows the directionality of the fluctuations when mean kinetic energy is transported. Hamilton *et al.* [26] and Viestenz and Cal [27] performed quadrant analysis on hot-wire anemometry measurements done in a wind tunnel in the wake of a 3×3 model wind farm. Both studies found that ejections and sweeps were primarily responsible for the vertical transport of mean kinetic energy. Lignarolo *et al.* [28] corroborated this conclusion by performing quadrant analysis on PIV measurements done on a single turbine in uniform flow. In the present study, the rotation of the model wind turbine blade is expected to impart characteristics to the spanwise fluctuating velocity component w' that are different from those imparted by a stationary disk. To capture the contribution of the spanwise velocity component, octant analysis is used rather than quadrant analysis.

III. EXPERIMENTAL DESIGN

Experiments are conducted at the facility at Portland State University. This closed-loop wind tunnel has a 9:1 contraction ratio. The test section has a 5 m length with a cross section $H \times W$ of 0.8×1.2 m^2. Figure 2 shows that a passive grid, strakes, and chains are placed upstream of the model wind farm in order to produce an inflow to the farm with characteristics that emulate the atmospheric boundary layer. The acrylic strakes used are identical in geometry to those employed by Cal *et al.* [21].

The model wind turbine array is composed of four rows of turbines in the streamwise direction as shown in Fig. 2. Each row is composed of three turbines with a cross-stream spacing of $3D$ from hub to hub. Three-bladed wind turbine models with the dimensions shown in Fig. 3(b) are used in this study and are compared to an array of matched porous disks shown in Fig. 3(c). Turbine blades are fabricated from 26-gauge (0.475-mm) galvanized steel sheet metal that is pressed via a die to give a twist of 15° at the blade tip and 22° at the blade root. Model nacelles are composed of an electric motor (Faulhaber GmbH model No. 1331T012SR) acting as a generator and loaded such that wind turbines are operating at their peak power coefficient C_p as described by Hamilton and Cal [29].

A matched set of 12 porous disks is built to compare with the rotors. Disks are laser cut from 3.2-mm-thick plywood. A rapid prototyped adapter is used to mount the disks to the nacelle in order to ensure that the downstream surface of the disk is at the same streamwise location as the rotor

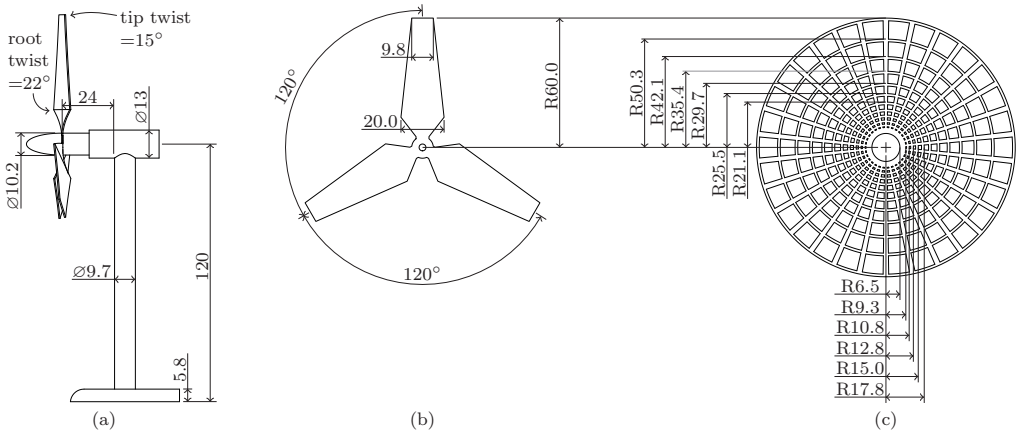

FIG. 3. Scale drawings of the geometry of the (a) turbine model with pressed rotor, (b) rotor flat pattern, and (c) porous disk. All dimensions are in millimeters unless otherwise noted. The mounting adapter for the hub of the disk is not shown.

hub. The disk was designed to be circumferentially symmetric with a porosity that varies with radial coordinate in order to mimic the design of the rotor.

The induction factor is used to match the disks to the rotor. An iterative procedure is applied to arrive at the particular disk design shown in Fig. 3(c). The induction factor is calculated from particle image velocimetry measurements of the flow field bracketing the center turbine in the first row. Velocity profiles were taken 23 mm upstream ($x/D = -0.19$) and 56 mm downstream ($x/D = 0.47$) of the rotor blade and disk, respectively. Linear interpolation between the upstream and downstream profiles was done to estimate the velocity profile at the disk and rotor, respectively. Velocity profiles pertinent to the disk characterization phase of the experiment are provided in Fig. 4. The induction factor a was then computed from this velocity profile following the method outlined in Cal *et al.* [21]. The method used by Cal *et al.* to compute a from the flow field relies upon the streamtube concept. This concept is expected to be most accurate when applied in the first row of turbines in the current setup, thus making the first turbine row the most appropriate location for disk characterization. As in Burton [30], the corresponding thrust coefficient C_t is computed from the induction factor via

$$C_t = 4a(1 - a). \tag{4}$$

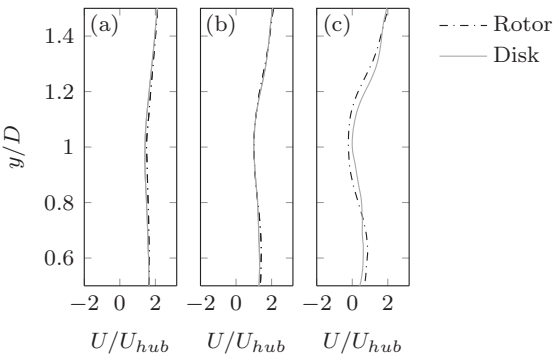

FIG. 4. Profiles of the rotor and disk found during characterization at the position of the first row. The streamwise location of the rotor or disk is $x/D = 0$: (a) measured profiles at $x/D = -0.19$, (b) computed profiles at $x/D = 0$, and (c) measured profiles at $x/D = 0.47$.

TABLE I. Comparison of disk and rotor characteristics.

Characteristic	Disk	Rotor
diameter (mm)	120	120
a	0.202	0.200
C_t	0.644	0.640

A summary of the disk and rotor characteristics are provided in Table I. Note that a and C_t are rounded to three significant digits and the percent difference between the induction factors of the disk and rotor is less than 1%. Furthermore, since disk and rotor matching is done in the first row of turbines, Eq. (4) has been applied in the absence of upstream turbine wakes.

Measurements are carried out using via stereo PIV (SPIV) upstream and downstream of the center turbine in the fourth row. Figure 2 shows the six SPIV planes surrounding the turbine of interest. Each individual plane $W \times H$ is approximately 165×240 mm^2. Measurement planes overlap by approximately $0.1D$. In regions where successive measurement planes overlap, the data from the two planes are averaged.

The SPIV system is composed of two LaVision 4-megapixel Pro LX cameras fitted with Schiempflug adapters, a Litron Nano L 200-15 double pulsed Nd:YAG laser, and the software DAVIS 8.1.5 by LaVision. The flow is seeded with diethylhexyl sebacate that was aerosolized through a seeding generator which uses a Laskin nozzle (LaVision model No. 1108926). Seeding densities throughout the field of view (FOV) of each camera are consistently held above 0.02 particles per pixel. The laser sheet thickness is 1–1.7 mm throughout the FOV of each camera. Cameras are placed in forward scatter with each camera viewing opposite sides of the laser sheet. The angle between each camera body and the laser sheet is 45° and thus the included angle between the two cameras is 90°. Calibration is done using a two-level calibration plate with markers placed at known locations. Self-calibration is performed on particles in the laser sheet using the method of Weineke [31] as implemented in DAVIS version 8.1.5. For each measurement plane, the disk and rotor measurements are carried out in series using the same camera and laser setup and the same camera calibration. Data are collected at a frequency of approximately 1 Hz. For each measurement plane, the time difference between image pairs δt is selected such that the maximum particle displacement in the measurement plane is 6 pixels. At each measurement plane, 3000 image pairs are collected in order to ensure statistical convergence for the disk and rotor cases, respectively.

Images are processed using a multigrid strategy for the stereo cross correlation with two passes with interrogation area size of 64×64 pixels with 50% overlap followed by three passes with an interrogation area size of 32×32 pixels. Erroneous vectors are removed using a median filter. Spurious vectors are replaced with vectors computed via interpolation from valid neighboring vectors. For all cases, fewer than 2% of vectors are removed and replaced. The uncertainty in the second-order statistics was found to be 3% [32].

IV. RESULTS AND DISCUSSION

A. Mean velocity components and mean kinetic energy

Figure 5 shows the mean velocity components and mean kinetic energy surrounding the center turbine in the fourth row of the array. Each subfigure is organized in a similar fashion with the top row of panels in the subfigure representing the rotor case and the bottom row of panels representing the disk case. The rotor hub and disk are located at $x/D = 0$ with the hub height located at $y/D = 1$. Figure 5(a) contains the normalized streamwise mean velocity component U/U_{hub}. In both cases, the upstream panels show the persistence of the wake generated from the third row of the array especially for $x/D \leqslant -2$. For $x/D \leqslant -2$, the corresponding downstream region below the top tip ($y/D = 1.5$) has values of U within 5%, which is consistent with previous studies indicating that

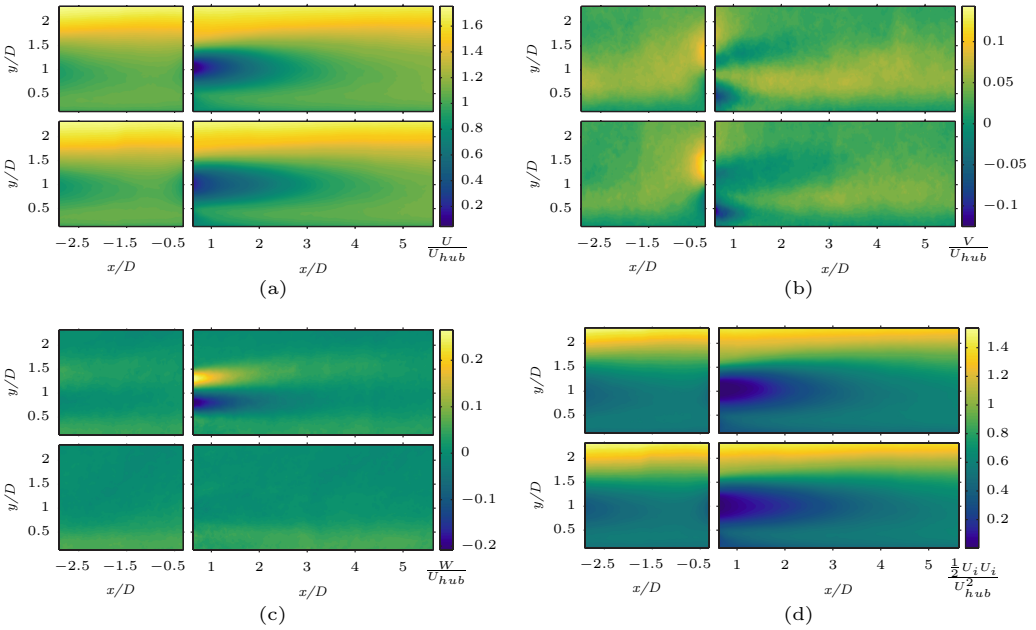

FIG. 5. Mean components of velocity and kinetic energy for the center turbine in the fourth row. In all subfigures, the inflow and wake of the rotor are in the top row, while the bottom row represents the porous disk. (a) Normalized streamwise mean velocity U/U_{hub}, (b) normalized wall normal mean velocity V/U_{hub}, (c) normalized spanwise mean velocity W/U_{hub}, and (d) normalized mean kinetic energy $(1/2)U_iU_i/U_{\text{hub}}^2$.

the turbine canopy boundary layer is fully developed by the fourth row in Cartesian turbine arrays [33]. Downstream of the model turbine, a velocity deficit is present in both cases at the hub height $y/D = 1$. While the rotor case shows a larger velocity deficit at the hub height and $x/D = 0.6$, it initially recovers at a higher rate so that by $x/D = 1.5$, the difference in U/U_{hub} between the rotor case and disk case is less than 10%. The similarity of the U component of the two cases is expected since the matching procedure that was employed is based on this quantity as highlighted in Sec. III.

Figure 5(b) presents the normalized vertical mean velocity component V/V_{hub}. Immediately upstream of both the disk and rotor (e.g., $x/D = 0.3$), positive values of V are present between the hub height and top tip as the flow moves upward as a result of the blockage created by the rotor and disk. The V component is up to 26% different for the rotor and disk cases between the hub height and the top tip at $x/D = 0.3$. Similarly, negative values of V are present for both cases between the hub height and bottom tip as the flow advects downward in response to the blockage of the rotor or disk. Between the hub height and top tip at streamwise coordinates $x/D < 1.5$, a region with negative values of V extends further downstream for the disk case than the rotor case.

The normalized spanwise mean velocity component in Fig. 5(c) shows the rotation in the rotor case, while no such rotational effects due to the disk are present since the disk is stationary. Especially for streamwise coordinates less than $3D$, positive values of W are found above the hub height where the rotor blade rotates into the measurement plane and negative values of W below the hub height where the blade rotates out of the measurement plane, thus conserving angular momentum. At $x/D = 0.6$, the differences in W between the disk and rotor cases are as large as 190% in the region between the top and bottom tip.

The mean kinetic energy K shown in Fig. 5(d) has contour lines of similar shape to those displayed for the U component. Comparing the magnitudes of U, V, and W in Fig. 5, it is evident that the maximum value of U is about an order of magnitude greater than either V or W. The larger magnitude of U relative to the other mean velocity components results in the U component

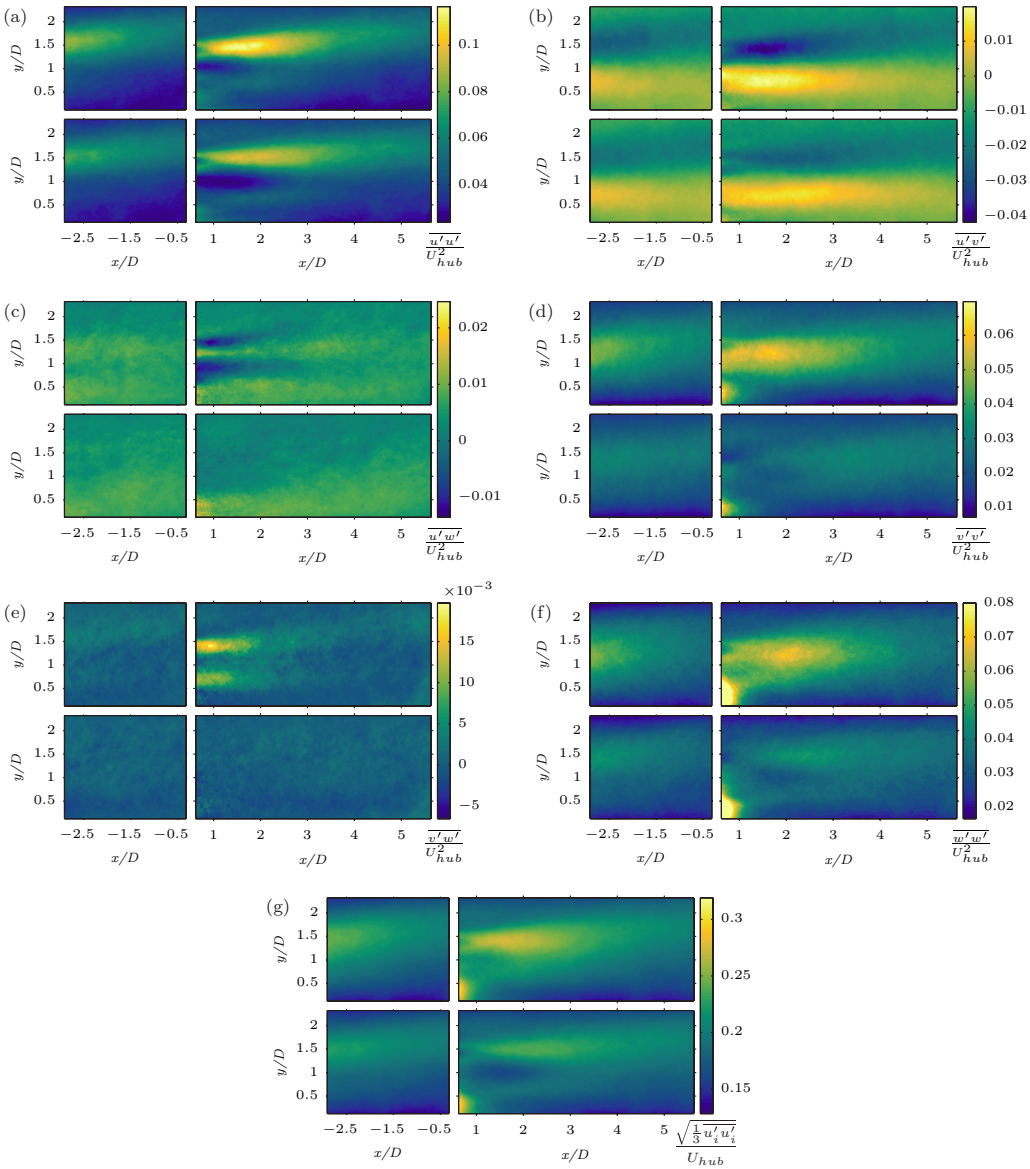

FIG. 6. Normalized time-averaged Reynolds stress tensor components $\overline{u'_iu'_j}/U^2_{\text{hub}}$ and turbulence intensity $\sqrt{(1/3)\overline{u'_iu'_i}}/U_{\text{hub}}$ where $i, j = 1,\ 2,$ or 3: (a) $\overline{u'u'}/U^2_{\text{hub}}$, (b) $\overline{u'v'}/U^2_{\text{hub}}$, (c) $\overline{u'w'}/U^2_{\text{hub}}$, (d) $\overline{v'v'}/U^2_{\text{hub}}$, (e) $\overline{v'w'}/U^2_{\text{hub}}$, (f) $\overline{w'w'}/U^2_{\text{hub}}$, and (g) $\sqrt{(1/3)\overline{u'_iu'_i}}/U_{\text{hub}}$. In each subfigure, the rotor case is represented in the top row while the disk case is represented in the bottom row.

dominating the behavior of K, with K defined as $K = 1/2(U^2 + V^2 + W^2)$. As a consequence, the trends described above for U are mirrored in K for both the rotor and disk cases.

B. Reynolds stresses and turbulence intensity

Figure 6 displays components of the time-averaged Reynolds stress tensor and the turbulence intensity, a quantity derived from the normal Reynolds stresses. The subfigures are organized

identically to those described in Sec. IV A with the rotor case in the top panels of each subfigure and the disk case in the bottom panels of each subfigure. For all components of the Reynolds stress tensor, the rotor case has a larger magnitude than the corresponding Reynolds stress component for the disk case for wall-normal distances between the top and bottom tips. This indicates that greater fluctuations from the mean flow are present in the rotor case than for the disk case. Below $y/D = 0.3$, the differences between the disk and rotor are $\leqslant 15\%$ for all components of the Reynolds stresses with the exception of $\overline{v'w'}$, which suggests that wall effects dominate the flow behavior at these heights.

The streamwise normal component of the Reynolds stress $\overline{u'u'}$ is illustrated in Fig. 6(a). While the overall shapes of the contours for $\overline{u'u'}$ are comparable, they differ in magnitude between the rotor and disk scenarios. In the near wake for both the rotor and disk cases, $\overline{u'u'}$ has a minimum at approximately the hub height $y/D \approx 1$. However, for the disk, this region with low values of $\overline{u'u'}$ is more elongated in the streamwise direction. Near the top tip $y/D = 1.5$, the maxima in $\overline{u'u'}$ occurs in both the rotor and disk. This larger maximum value for the rotor occurs at $x/D = 1.6$ and is 22% greater than the disk case at the same coordinates.

Figure 6(b) shows the in-plane Reynolds shear stress $\overline{u'v'}$, which physically represents the vertical flux of momentum. Negative values of $\overline{u'v'}$ indicate a downward flux of momentum, whereas positive values indicate an upward flux of momentum. For both the rotor and disk, $\overline{u'v'}$ changes sign at approximately the hub height throughout the measured region downstream of the fourth row. This sign change is present upstream of the fourth row in the segment of the wake that persists from the third row. From approximately the bottom tip to the hub height, the values of $\overline{u'v'}$ are positive, which demonstrates an upward momentum flux in this region. On the other hand, from the hub to $y/D = 2.3$, the topmost measurement point, the momentum flux is downward from the higher momentum fluid above the canopy of the array. The magnitudes of $\overline{u'v'}$ differ between the rotor and disk case in the near wake particularly for $x/D \leqslant 2.8$, where the maxima and minima are more extreme for the rotor. The minimum value of the in-plane shear stress for the rotor of occurs just below the top tip at $y/D = 1.45$ at a streamwise coordinate of $x/D = 1.54$ and is 51% different from the value for the disk case at the same spatial coordinates. The maximum of $\overline{u'v'}$ for the rotor wake occurs at $y/D = 0.75$ and a streamwise coordinate of $x/D = 1.6$ and is 40% greater than the value for the disk case at the corresponding location.

Figure 6(c) presents $\overline{u'w'}$, which demonstrates, for $x/D \lesssim 2$, a pattern of alternating of signs between the bottom and top tip only for the rotor case. This pattern and its implications are further investigated through octant analysis in Sec. IV F. For these streamwise coordinates, just below the top tip, the sign of $\overline{u'w'}$ is negative, signifying that u' and w' have opposite signs. The shear stress $\overline{u'w'}$ is positive over a narrow feature, which for $x/D = 0.6$ occurs between $1.4 \leqslant y/D \leqslant 1.1$, indicating that u' and v' have the same sign in this band. A more extended region having negative values of $\overline{u'w'}$ is then present from the hub height to the bottom tip. Within the two regions in which this shear stress is negative, the observed values of $\overline{u'w'}$ for the rotor and disk cases differ by as much as 200%.

Like $\overline{u'w'}$, the component $\overline{v'w'}$, shown in Fig. 6(e), has an evident pattern in the rotor case only. However, in the near wake, $\overline{v'w'}$ does not have regions of alternating signs of the stress as in $\overline{u'w'}$. Instead, $\overline{v'w'}$ has two areas of higher magnitude and positive sign just below the top tip and just above the bottom tip. Positive values of this shear stress signify that v' and w' have the same sign. For the same streamwise coordinate, the Reynolds shear stress component $\overline{v'w'}$ is 1.5–2 times greater in the band at the top tip in comparison to the band near the bottom tip. Between these two areas, approaching nacelle height, this stress decreases by one to two orders of magnitude.

Figures 6(d) and 6(f) display the wall-normal Reynolds stress $\overline{v'v'}$ and the spanwise Reynolds stress $\overline{w'w'}$, respectively. Both normal stresses show the effect of the turbine tower particularly where $x/D \leqslant 1$ and $y/D \leqslant 0.7$. The rotor case exhibits higher values for both stresses than the disk case, especially heights between the bottom and top tips and streamwise coordinates $x/D \leqslant 3.5$. The maximum difference between the rotor and disk is 97% for $\overline{v'v'}$, which occurs at $x/D = 0.62$ and $y/D = 1.42$. For $\overline{w'w'}$, the largest difference between the rotor and disk is 70%, which is present at $x/D = 1.87$ and $y/D = 1.02$.

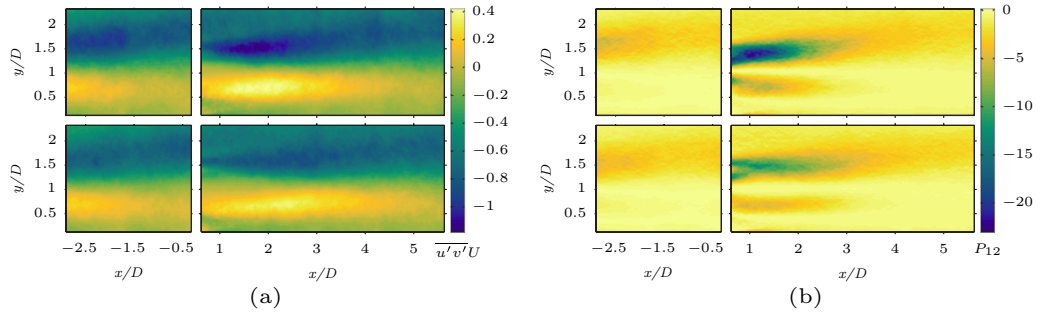

FIG. 7. Largest magnitude components (a) relating to the vertical flux of mean kinetic energy $\overline{u'v'}U$ and (b) of the production of turbulent kinetic energy tensor $P_{12} = \overline{u'v'}(\partial U/\partial y)$. The inflow and wake of the rotor are in the top row of each subfigure, while the bottom panels represent the porous disk. Units are $m^3\,s^{-3}$ and $m^2\,s^{-3}$ for $\overline{u'v'}U$ and P_{12}, respectively.

The turbulence intensity Tu based on U_{hub} is shown in Fig. 6(g). The turbulence intensities of the disk and rotor cases are qualitatively similar in that both exhibit a region of elevated Tu immediately downstream of the tower particularly $y/D \leqslant 0.4$ and a second region of elevated Tu in the vicinity of the top tip ($y/D = 1.5$). In the area immediately downstream of the tower and at wall-normal locations $y/D \leqslant 0.4$, the difference between the rotor and disk cases are below 1%. However, in the vicinity of the top tip, the rotor case exhibits higher turbulence intensities than the disk case, which reach a maximum of 26% at $x/D = 0.6$ and then decrease and remain in the range of 15%–19% for $1 \leqslant x/D \leqslant 2$ followed by a monotonic decrease to 7% by $x/D = 3$ and 4% by $x/D = 4$. The largest differences in Tu are found bracketing the hub height particularly for $1.2 \lesssim x/D \lesssim 2.3$, where the disk case exhibits lower turbulence intensities than the rotor case. The maximum difference in this region is 33% at coordinate $(x/D, y/D) = (1.8, 1.1)$. Since the turbulence intensity based on U_{hub} is represented as $\text{Tu} = \sqrt{(1/3)(\overline{u'u'} + \overline{v'v'} + \overline{w'w'})}/U_{\text{hub}}$, the features of the turbulence intensity fields of the rotor and disk are derived from their respective Reynolds normal stresses. For example, the area of elevated turbulence intensity immediately downstream of the tower for $y/D \leqslant 0.4$ is mirrored in $\overline{w'w'}$ and to a lesser degree in $\overline{v'v'}$ for both the rotor and disk cases.

C. Vertical mean kinetic energy flux and production of TKE

Figure 7(a) illustrates the largest term related to the vertical flux of mean kinetic energy $\overline{u'v'}U$ for the rotor and disk. This figure is organized in a way that is identical to figures found in Secs. IV A and IV B with the rotor in the top panels and the disk in the bottom panels. Other components of $\overline{u_i'u_j'}U_i$, where $i = 1$, 2, or 3 and $j = 2$, are smaller by an order of magnitude or more. Given the similarity in U for the disk versus the rotor described in Sec. IV A, the differences in $\overline{u'v'}U$ between the two cases primarily arise from $\overline{u'v'}$, as described in Sec. IV B. Thus, the same trends described in $\overline{u'v'}$ in Fig. 6(b) are also present in $\overline{u'v'}U$ in Fig. 7(a). Cal *et al.* [21] estimated the net vertical flux of kinetic energy into a control volume bounded by the top and bottom rotor tips and found that the result was of the same order of magnitude as the power extracted by the turbine. Notably, in this method, the net kinetic energy flux is proportional to the difference in $\overline{u'v'}U$ between the top and bottom rotor tips. In the present experiment, the difference in streamwise spatial averages is $\langle -\overline{u'v'}U\rangle_x|_{y/D=1.5} - \langle -\overline{u'v'}U\rangle_x|_{y/D=0.5}$, which is 0.91 $m^3\,s^{-3}$ for the rotor case and 0.79 $m^3\,s^{-3}$ for the disk case, representing a difference of 13%. The net vertical mean kinetic energy flux for the disk and rotor would be expected to follow this same trend, suggesting a greater net vertical flux for the rotor than the disk.

The most significant component of the production of TKE term, $\overline{u'v'}(\partial U/\partial y)$, is represented in Fig. 7(b). Considering only measurement locations downstream of the fourth row, the global average

of $\overline{u'v'}(\partial U/\partial y)$ is three times greater than the next component closest is magnitude and an order of magnitude greater than the remaining components. For both the rotor and the disk, regions of high magnitude production occur at the top tip with a less intense feature just above the bottom tip. Elsewhere, production is close to zero. The sign of $\overline{u'v'}(\partial U/\partial y)$ is negative in both of these bands, indicating that kinetic energy is being extracted from the mean flow. Especially for $x/D < 2.5$, the rotor case exhibits higher absolute values of production with the maximum at the top tip at a streamwise coordinate of $x/D = 1.1$. Here the greater absolute value of $\overline{u'v'}(\partial U/\partial y)$ for the rotor is 87% different from the corresponding absolute value for disk. These high production areas likely arise from vortex breakdown. Interaction of vortices shed at the bottom tip with the tower would be expected to cause production of TKE to be of a smaller magnitude near the bottom tip.

D. Determining the region in the wake where rotation is of most importance

The most evident difference between the rotor and disk cases is due to the rotation of the rotor, which is shown in the mean spanwise velocity component W in Fig. 5(c). Thus, the mean kinetic energy budget is analyzed by separating the downstream measurements into two segments based on W. The criterion for determining the location at which to divide the downstream measurements was made by evaluating the vertical average of the absolute value of W represented as $\langle|W|\rangle_y$ between the top tip ($y/D = 1.5$) and bottom tip ($y/D = 0.5$). Thereafter, the derivative of $\langle|W|\rangle_y$ with respect to the streamwise coordinate was obtained using a second-order central differencing scheme to yield $d\langle|W|\rangle_y/dx$. After a steep change in magnitude in the region $0.6 \leqslant x/D \lesssim 3$, $d\langle|W|\rangle_y/dx$ oscillates about zero by the streamwise coordinate $x/D \approx 3$. This indicates that only small changes in W occur for $x/D \gtrsim 3$. These trends are evident in Fig. 4(c). Due to the amplification of noise in W from the computation of the derivative, a polynomial line of best fit of $d\langle|W|\rangle_y/dx$ was utilized to aid in a precise determination of the streamwise coordinate at which $d\langle|W|\rangle_y/dx$ reaches a near constant value. Based on the line of best fit, this streamwise coordinate is $x/D = 3.2$. Given these changes in $\langle|W|\rangle_y$ as a function of the streamwise coordinate, the region $0.6 \leqslant x/D \leqslant 3.2$ represents the region of the wake where rotation is most important, while the region $3.2 < x/D \leqslant 5.6$ delineates the region where rotation is less important.

E. Mean kinetic energy budget as a function of rotational effects

The terms in the mean kinetic energy budget are computed and horizontally averaged in the two regions $0.6 \leqslant x/D \leqslant 3.2$ and $3.2 < x/D \leqslant 5.6$ to create the vertical profiles shown in Fig. 8. Components requiring partial derivatives with respect to z are not included nor is the term representing transport due to the local pressure gradient depicted. The dissipation term $2\nu S_{ij}S_{ij}$ and the term representing transport due to viscosity $2\nu\partial S_{ij}U_i/\partial x_j$ are of order 10^{-3} and 10^{-2} or less, respectively. Thus, both of these quantities appear to be zero on the scale used in Fig. 8.

The wall-normal location of the peak values represented in Fig. 8 for the rotor and disk are within $0.06D$ of one another. In the vicinity of the top tip, the peak value of advection $U_j\partial K/\partial x_j$ for the rotor is $-16.4\,\mathrm{m^2\,s^{-3}}$ at $y/D = 1.68$ and $-14.7\ \mathrm{m^3\,s^{-3}}$ at $y/D = 1.73$ for the disk, which represents a difference of 11%. Recall that $K = 1/2(\overline{U_iU_i})$, where $i = 1$, 2, or 3. Also near the top tip, the term representing transport via turbulence $\partial\overline{u_i'u_j'}U/\partial x_j$ is 28% different between the rotor and disk with peak values in $0.6 \leqslant x/D \leqslant 3.2$, while the percent difference in the peak values for the disk and rotor is 6% for $3.2 < x/D \leqslant 5.6$. Similar trends are observed for peak values near the top tip for the production term $\overline{u_i'u_j'}\partial U_i/\partial x_j$, which are 41% different in $0.6 \leqslant x/D \leqslant 3.2$ and 2% different in $3.2 < x/D \leqslant 5.6$. For heights between the top and bottom tips, the difference in the peak value of the advection term for $0.6 \leqslant x/D \leqslant 3.2$ is 28%, which decreases to a difference of 7% in $3.2 < x/D \leqslant 5.6$. Also between the bottom and top tips, the difference in the term representing transport via turbulence is 45% in $3.2 < x/D \leqslant 5.6$, which declines to a difference of 6% in $3.2 < x/D \leqslant 5.6$. Thus, while significant percent differences are present in the region where rotation is most important ($0.6 \leqslant x/D \leqslant 3.2$), these differences are mitigated in the region where

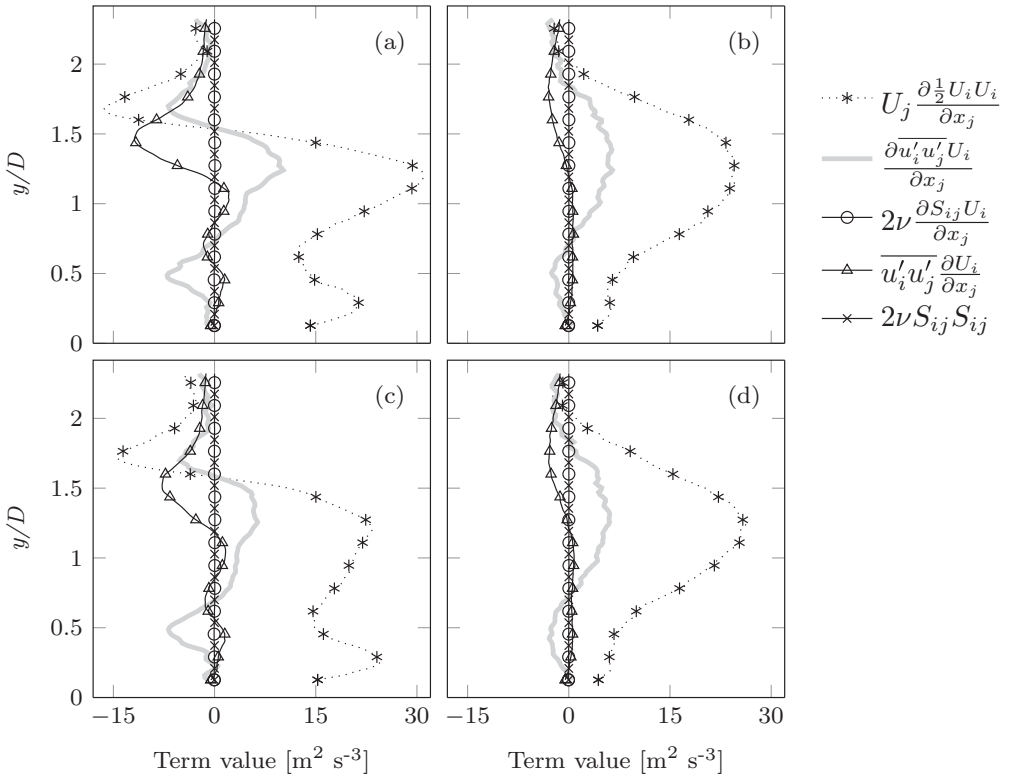

FIG. 8. Horizontal averages of terms in the mean kinetic energy budget in the region where rotation is most important, $0.6 \leqslant x/D \leqslant 3.2$, for the (a) rotor and (c) disk. Also shown are the corresponding horizontal averages in the region where rotation is less important, $3.2 < x/D \leqslant 5.6$, for the (b) rotor and (d) disk.

rotation is less important ($3.2 < x/D \leqslant 5.6$) to the extent that the mean kinetic energy transport terms are nearly equivalent in the region where rotation is less important.

F. Conditional averaging of $\overline{u'v'}U$ via octant analysis

Octant analysis of $\overline{u'v'}U$ yields the conditionally averaged quantity $\overline{u'v'U}$, which is shown in Fig. 9. Figures 9(a) and 9(b) represent the rotor in the near and far wakes, respectively. Similarly, Figs. 9(c) and 9(d) illustrate the disk for the near and far wakes, respectively. Furthermore, the arrangement of the eight panels in each subfigure corresponds to the variation in the signs of u', v', and w' shown in Fig. 1. This conditional averaging was done as outlined in Eq. (2). The summation of $\overline{u'v'U}$ over all eight octants in Fig. 9(a) yields $\overline{u'v'}U$, shown in Fig. 6(a) for $0.6 \leqslant x/D \leqslant 2$. The same summation can be done over all octants for $\overline{u'v'U}$ in the far wake of the rotor case shown in Fig. 9(b) and for the disk case in Figs. 9(c) and 9(d) to arrive at the corresponding values of $\overline{u'v'}U$.

Octant analysis for the rotor case corroborates and also extends previous work in quadrant analysis of wind turbine wakes [26,27]. These previous works showed that ejections ($u' < 0$ and $v' > 0$) and sweeps ($u' > 0$ and $v' < 0$) dominate the vertical mean kinetic energy transport into the swept area of the rotor. Viestenz and Cal [27] found a maximum for ejections just above the top tip and a maximum for sweeps just below the top tip. Both of these maxima contribute to vertical kinetic energy flux. In the present work, octant analysis reveals the role that w' plays in ejections ($O2$ and $O5$) and sweeps ($O4$ and $O8$) in the vicinity of the top tip. For the rotor case, a maximum in

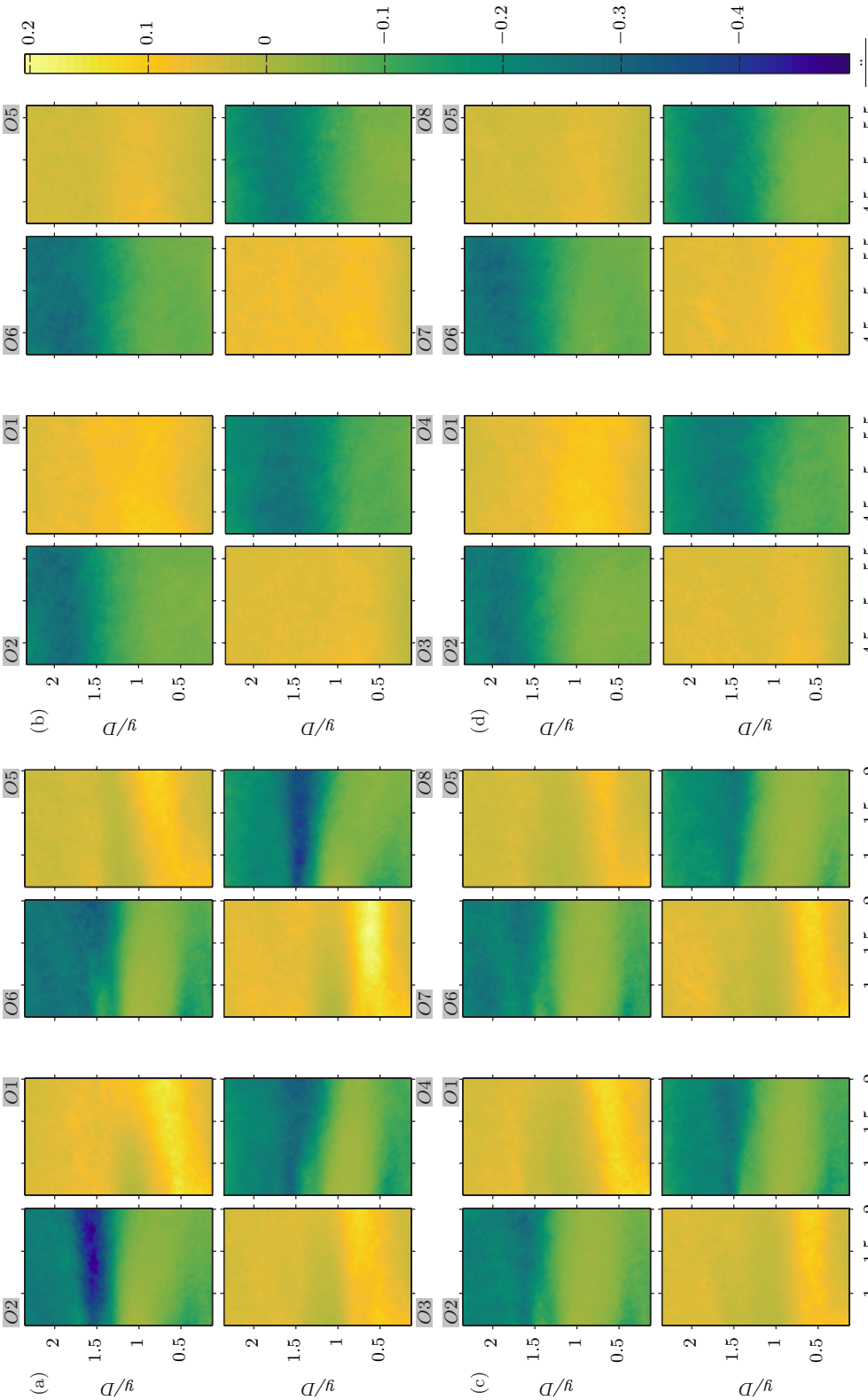

FIG. 9. Conditional averages of the vertical mean kinetic energy flux $\overline{u'v'U}$ for each octant. Rotor results are given for (a) the near wake and (b) the far wake. Results for the disk are provided in (c) the near wake and (d) the far wake. (a)–(d) all have a common arrangement of eight panels organized according to the signs of u', v', and w' as in Fig. 1. Octants 1–4 have positive signs of w', while octants 4–8 have negative signs of w'.

the magnitude of $\overline{\ddot{u'v'U}}$ is present at the top tip in Fig. 9(a) for ejections. However, it is primarily ejections in $O2$, which have a positive sign for w', that contribute to this maximum for the rotor case. Ejections in $O2$ represent situations where the direction of w' is in the direction opposite that of the rotor rotation at the top tip. Similarly, a maximum is found just below the top tip in Fig. 9(a) for sweeps in the rotor case. This maximum is dominated by sweeps in $O5$, which possess a negative sign for w'.

The observation in the rotor case that ejections at the top tip have a preference for $O2$ while sweeps at the top tip have a preference for $O8$ is in accord with patterns found in the Reynolds shear stresses $\overline{u'w'}$ and $\overline{v'w'}$ (see Sec. IV B). Specifically, the presence of top tip ejections in $O2$, where $u' < 0$ and $w' > 0$, and top tip sweeps in $O8$, where $u' > 0$ and $w' < 0$, agrees with the negative sign of $\overline{u'w'}$ observed at the top tip in Fig. 6(c). This octant preference for top tip ejections and sweeps is also in agreement with the positive sign of $\overline{v'w'}$ at this location for the rotor in Fig. 6(e). Although the maximum positive value of $\overline{v'w'}$ is found just below the top tip, this region in which $\overline{v'w'}$ is positive extends above the rotor tip.

One physical mechanism that would cause a preference for a specific sign of w' for sweeps and ejections near the top tip is related to the periodic nature of the blockage by the rotor. As the blade passes through its topmost position and is within the PIV plane, blockage by the blade would be expected to tend to reduce the instantaneous local streamwise velocity to a value smaller than the ensemble average U leading to a negative value of u'. Since fluctuations are centered about the mean, any instantaneous velocity smaller than the ensemble mean corresponds to a negative value of the fluctuation, while an instantaneous velocity greater than the ensemble average generates a positive value of the fluctuation. Furthermore, the position of the blade in the PIV plane would tend to cause the value of the instantaneous vertical velocity near the top tip to be larger than the ensemble average V as the flow is deflected upward over the blade tip leading to a positive deviation of v'. At this same point in time, the instantaneous spanwise velocity measured in the PIV plane would be expected to be larger than the ensemble average W due to the close proximity of the blade and angular velocity imparted by the blade. Such a tendency for larger instantaneous values of the spanwise velocity would lead to positive values of w'. This combination of signs for the velocity fluctuations produces sweeps in $O2$ and may explain why ejections in $O2$ are more predominant than ejections in $O6$ in the vicinity of $y/D = 1.5$.

In contrast, when the rotor blade has passed its topmost position, the absence of a blockage in the PIV plane would be expected to tend to cause streamwise velocities near the top tip to have instantaneous values that are larger than U leading to positive values of u'. Similarly, the absence of the blade would tend to produce instantaneous vertical velocities that are lower than V since the flow is not deflected by the blade. These instantaneous vertical velocities that are smaller than V correspond to negative values of v'. Concurrently, the absence of the blade at its topmost position would be tend to lead to instantaneous spanwise velocities locally that are smaller than W due to the lack of rotational influence of the blade. Instantaneous spanwise velocities that are smaller than W correspond to negative values of w'. This combination of the signs of the fluctuations leads to sweeps in $O8$ and may provide insight as to why sweeps at the top tip in $O8$ are more dominant than those in $O2$. The relative vertical displacement of the maxima near top tip for ejections and sweeps is also consistent with this physical mechanism.

Two trends are present in Fig. 9. One trend is that the disparities between $\overline{\ddot{u'v'U}}$ in the same octant for the rotor versus the disk decrease moving from the near wake to the far wake. For example, compare $\overline{\ddot{u'v'U}}$ in $O2$ for the rotor in the near wake in Fig. 9(a) with $O2$ for the disk in the near wake shown in Fig. 9(c), especially near the top tip $y/D = 1.5$. Second, for the rotor case itself, differences between octants with the same sign of u' and v' but opposite signs of w' also decrease in moving from the near wake to the far wake. For example, compare $O2$ with $O6$ in the near wake in Fig. 9(a) and then compare $O2$ with $O6$ in the far wake in Fig. 9(b). Significant variations in $\overline{\ddot{u'v'U}}$ between such corresponding octants in the rotor case in the near wake indicate that a strong preference for a particular sign of w' is associated with vertical mean kinetic energy flux and that this

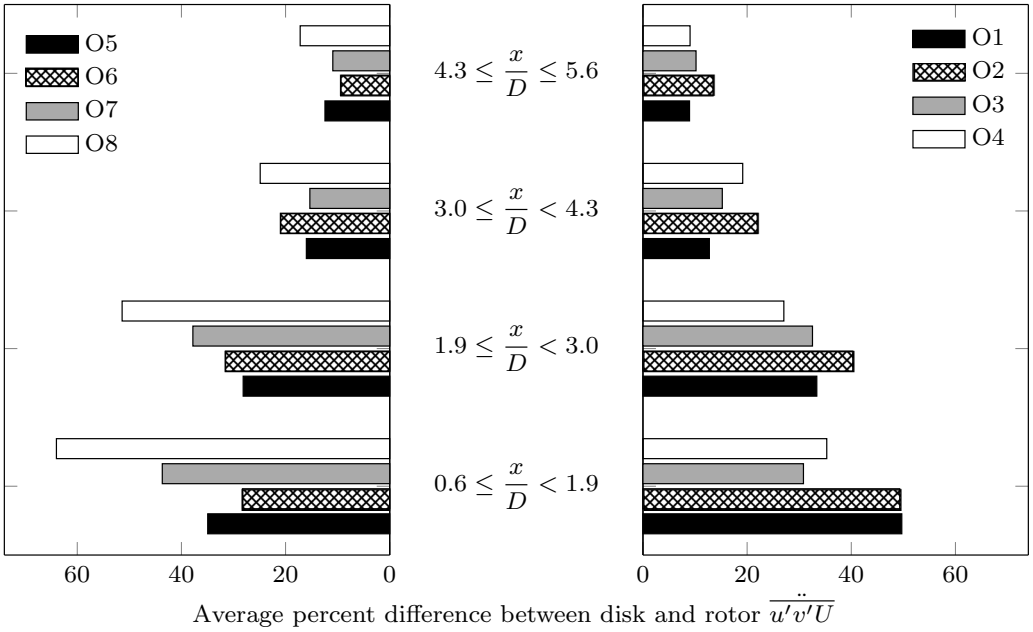

FIG. 10. Average percent difference between $\overline{\ddot{u'v'U}}$ for the disk and rotor in each octant as a function of downstream streamwise distance. Only data between the top ($y/D = 1.5$) and bottom tips ($y/D = 0.5$) are considered. As the downstream distance increases, differences decrease and the average percent difference becomes more symmetric with respect to the sign of w'.

preference is related to the rotation of the rotor. Two features of Fig. 9 suggest that the rotationality of the rotor does not heavily impact vertical mean kinetic energy transport in the far wake: (1) the absence of a strong preference for a particular sign of w' illustrated by the comparable values of $\overline{\ddot{u'v'U}}$ found between corresponding octants in the far wake in the rotor case and (2) the agreement between the rotor and disk octants in the far wake.

Since $\overline{\ddot{u'v'U}}$ is related to the vertical transport of mean kinetic energy, inferences can be made regarding transport from these results. Specifically, these observations point towards the idea that the instantaneous directionality of the fluctuations that lead to vertical kinetic energy transport are quite different in the region nearest the turbine where rotation is important and are then minimized in the far wake. In addition, these results imply a difference in the flow structure that occurs concurrently with vertical mean kinetic transport in the near wake and a curtailment of these flow structure differences associated with transport in the far wake.

A quantitative comparison of the octant analysis results for the rotor and disk cases as a function of downstream streamwise distance is shown in Fig. 10 . From the octant analysis of $\overline{\ddot{u'v'U}}$ for each of the downstream PIV planes, the percent difference at every measurement point between $\overline{\ddot{u'v'U}}$ for the disk and rotor in each octant was calculated. For the region between the top and bottom tips, the resulting percent differences of $\overline{\ddot{u'v'U}}$ in each octant were then averaged to arrive at the average percent differences displayed in Fig. 10. This method was applied to each of the four downstream PIV measurement planes. The average percent differences between the same octant for the rotor and disk decrease from a maximum of 68% in $0.6 \leqslant x/D \leqslant 1.9$ to a maximum of 17% in the furthest downstream plane ($4.3 \leqslant x/D \leqslant 5.6$). The asymmetry of these average percent differences decreases moving downstream, which can be seen by comparing octants with the same signs of u' and v' but differing signs of w'. For example, compare the magnitude of the averages in $O3$ versus $O7$ at streamwise coordinates $0.6 \leqslant x/D \leqslant 1.9$ to those in $O3$ versus $O7$ at streamwise coordinates

$4.3 \leqslant x/D \leqslant 5.6$. This reduction in asymmetry moving downstream indicates decreased preference for a particular sign of w'.

V. CONCLUSION

Within a model wind farm, the wake of a model turbine with a three-bladed rotor is compared to the wake produced by a matched porous disk. The mean velocity components, Reynolds stresses, mean kinetic energy budget, and an octant analysis of the term most relevant to vertical transport of mean kinetic energy are used to make a detailed comparison of the flow physics in the two cases. The main difference in the mean velocity components is found to be the W component, which results from rotation of the rotor. The Reynolds normal stresses share the same features for the rotor and disk, although normal stresses have consistently higher magnitudes for the rotor between the top and bottom tips, especially for $x/D \leqslant 3.5$. The same comments apply for the shear stress $\overline{u'v'}$. The variation in the normal stresses leads to a higher turbulence intensity in this area for the rotor than the disk. In contrast, shear stresses involving w' have altogether different patterns of features for the disk and rotor in the near wake.

Discrepancies between the rotor and disk cases in terms of the normal stresses and thus the turbulence intensity are noteworthy because of the potential impact on the inflow of downwind turbines. The dynamic loads and fatigue characteristics of wind turbines are impacted by the turbulence intensity of the inflow [5]. Furthermore, modification of the turbine structural support to account for turbulence intensity increases caused by upstream wakes had been found to be advantageous under some circumstances in offshore farms [34]. Turbine control schemes are also related to the inflow of turbines throughout the wind farm [35,36]. The present results suggest that the reduced normal stresses and turbulence intensity observed in the disk case are primarily a concern for scenarios in which a stationary disk parameterization for the rotor is used in computational simulations of farms where the spacing is less than $3-4D$. However, this specific spacing would be influenced by atmospheric conditions since atmospheric conditions have been found to impact wake recovery and modulate the inflow to downstream turbines [37]. Some operational wind farms such as Middelgrunden have a turbine spacing that is within this $3D-4D$ range [38]. However, the present results suggest that farms with turbine-to-turbine spacings larger than $3D-4D$ would be adequately represented using rotor parameterizations that involve a stationary disk if the quantity of interest is primarily influenced by the turbine inflow.

Examining the W component for the rotor case, rotational effects are evident particularly in the region $0.6 \leqslant x/D \leqslant 3.2$ and are absent in the disk case. In this same region where rotation has the greatest influence, differences in the peak values of mean kinetic energy transport terms are as large as 41% percent different to as small as 3% different. In contrast, in the region where rotation was found to be less important, percent differences in the peak values of the mean kinetic energy transport terms were found to range from a percent difference of 6% at most to 2% at the least. In the segment of the wake where rotation is most important, the greatest disparities are found in the production of the TKE term in the vicinity of the top tip. In comparison to the disk, the rotor case has a greater production of TKE, indicating that more kinetic energy is extracted from the mean flow in the swept area of the rotor. However, this efflux of mean kinetic energy in the rotor case is offset by a greater transport of kinetic energy by turbulence. Thus, in the region of the wake where rotation is less important, the terms in the mean kinetic energy equation are nearly equivalent, while significant discrepancies exist where rotation is a crucial characteristic.

Conditional averaging of $\overline{u'v'U}$ to obtain $\overline{u'v'U}$ using an octant analysis approach is done in order to examine the directionality of the velocity fluctuations from the mean that are associated with the vertical flux of mean kinetic energy. At measurement locations nearest the turbine model, evident preferences for certain signs of w' are present in the rotor case and are minimized in the disk case. Such a preference is particularly apparent at the rotor top tip where the maximum magnitude of $\overline{u'v'U}$ is found in octant 2 where $w' > 0$. In contrast, just below the top tip for the rotor, the

maximum magnitude of $\overline{\overline{u'v'U}}$ is found in octant 8 where $w' < 0$. Disparities in $\overline{\overline{u'v'U}}$ between the rotor and disk in the same octant are an indication that the flow structures associated with vertical mean kinetic energy flux are different in the near wake for the rotor than for the disk. However, such differences are not as evident in the far wake.

The mean kinetic energy budget and octant analysis suggest that rotor and disk cases interact with the atmosphere aloft distinctly differently in the region of the wake where rotation is a key flow feature. The mean kinetic energy budget indicates that the vertical entrainment of mean kinetic energy from the fluid above the farm at the top tip is lower in the disk case than in the rotor case. Octant analysis indicates that the mechanism responsible for this entrainment is dissimilar for the rotor and disk cases. However, determining the details of this mechanism requires elucidation of the flow structure responsible. Together, these two analyses imply that studies that seek to examine the details of the interaction of farms with the atmosphere would benefit from a rotor parameterization that represents rotational effects.

The comparable nature of the results using the present two mean kinetic energy analysis techniques points to the idea that the flow is nearly the same from the perspective of the mean velocity and mean kinetic energy equation in regions where rotation is not a critical phenomenon. To extend these results to modeling applications, it is important to consider that the inflow conditions and simulated atmospheric conditions would be expected to heavily impact the extent of the wake that is highly influenced by rotation. For example, in highly turbulent and convective atmospheric conditions, this region would be expected to be shorter than in conditions that were more quiescent. Thus, a criterion akin to the one applied in the present work would be advantageous in order to apply the present conclusions in other scenarios. Overall, these results are encouraging for modelers who employ the actuator disk model for simulations of wind farms and are therefore addressing questions that are related to the mean energetics of the flow.

ACKNOWLEDGMENTS

Vasant Vuppuluri is acknowledged for his help in disk characterization and experimental set up. This work was funded by the National Science Foundation (NSF-CBET-1034581).

[1] Global Wind Report 2015, http://www.gwec.net/wp-content/uploads/vip/GWEC-Global-Wind-2015-Report_April-2016_22_04.pdf.

[2] L. P. Chamorro and F. Porté-Agel, A wind-tunnel investigation of wind-turbine wakes: Boundary-layer turbulence effects, Bound.-Lay. Meteorol. **132**, 129 (2009).

[3] R. J. Barthelmie, S. C. Pryor, S. T. Frandsen, K. S. Hansen, J. G. Schepers, K. Rados, W. Schlez, A. Neubert, L. E. Jensen, and S. Neckelmann, Quantifying the impact of wind turbine wakes on power output at offshore wind farms, J. Atmos. Ocean. Technol. **27**, 1302 (2010).

[4] N. Hamilton, M. Melius, and R. B. Cal, Wind turbine boundary layer arrays for Cartesian and staggered configurations-Part I, flow field and power measurements, Wind Energy **18**, 277 (2015).

[5] W. Tian, A. Ozbay, and H. Hu, Effects of incoming surface wind conditions on the wake characteristics and dynamic wind loads acting on a wind turbine model, Phys. Fluids **26**, 125108 (2014).

[6] S. Lee, M. Churchfield, P. Moriarty, J. Jonkman, and J. Michalakes, *50th AIAA Aerospace Sciences Meeting*, AIAA Paper 2012-0540 (AIAA, Reston, VA, 2012).

[7] W. Zhang, C. D. Markfort, and F. Porté-Agel, Experimental study of the impact of large-scale wind farms on land-atmosphere exchanges, Environ. Res. Lett. **8**, 015002 (2013).

[8] S. B. Roy and J. J. Traiteur, Impacts of wind farms on surface air temperatures, Proc. Natl. Acad. Sci. USA **107**, 17899 (2010).

[9] L. J. Vermeer, J. N. Sørensen, and A. Crespo, Wind turbine wake aerodynamics, Prog. Aerosp. Sci. **39**, 467 (2003).
[10] B. Sanderse, S. P. van der Pijl, and B. Koren, Review of computational fluid dynamics for wind turbine wake aerodynamics, Wind Energy **14**, 799 (2011).
[11] J. N. Sørensen, Aerodynamic aspects of wind energy conversion, Annu. Rev. Fluid Mech. **43**, 427 (2011).
[12] Y.-T. Wu and F. Porté-Agel, Large-eddy simulation of wind-turbine wakes: Evaluation of turbine parametrisations, Bound.-Lay. Meteorol. **138**, 345 (2011).
[13] L. A. Martínez-Tossas, M. J. Churchfield, and S. Leonardi, Large eddy simulations of the flow past wind turbines: Actuator line and disk modeling, Wind Energy **18**, 1047 (2015).
[14] P.-Å. Krogstad and P. E. Eriksen, Blind test calculations of the performance and wake development for a model wind turbine, Renew. Energy **50**, 325 (2013).
[15] F. N. Coton, T. Wang, and R. A. M. Galbraith, An examination of key aerodynamic modeling issues raised by the NREL blind comparison, Wind Energy **5**, 199 (2002).
[16] S. Schreck, The NREL full-scale wind tunnel experiment: Introduction to the special issue, Wind Energy **5**, 77 (2002).
[17] S. Aubrun, S. Loyer, P. E. Hancock, and P. Hayden, Wind turbine wake properties: Comparison between a non-rotating simplified wind turbine model and a rotating model, J. Wind Eng. Ind. Aerodyn. **120**, 1 (2013).
[18] L. E. M. Lignarolo, D. Ragni, C. J. Simão Ferreira, and G. J. W. van Bussel, Kinetic energy entrainment in wind turbine and actuator disk wakes: An experimental analysis, J. Phys.: Conf. Ser. **524**, 012163 (2014).
[19] R. J. Barthelmie and L. E. Jensen, Evaluation of wind farm efficiency and wind turbine wakes at the Nysted offshore wind farm, Wind Energy **13**, 573 (2010).
[20] M. Calaf, C. Meneveau, and J. Meyers, Large eddy simulation study of fully developed wind-turbine array boundary layers, Phys. Fluids **22**, 015110 (2010).
[21] R. B. Cal, J. Lebrón, L. Castillo, H. S. Kang, and C. Meneveau, Experimental study of the horizontally averaged flow structure in a model wind-turbine array boundary layer, J. Renew. Sustain. Energy **2**, 013106 (2010).
[22] M. Abkar and F. Porté-Agel, Mean and turbulent kinetic energy budgets inside and above very large wind farms under conventionally-neutral condition, Renew. Energy **70**, 142 (2014).
[23] J. M. Wallace, H. Eckelmann, and R. S. Brodkey, The wall region in turbulent shear flow, J. Fluid Mech. **54**, 39 (1972).
[24] S. M. Ölçmen, R. L. Simpson, and J. W. Newby, Octant analysis based structural relations for three-dimensional turbulent boundary layers, Phys. Fluids **18**, 025106 (2006).
[25] M. M. Madden, Jr., Octant analysis of the Reynolds stresses in the three dimensional turbulent boundary layer of a prolate spheroid, Ph.D. thesis, Virginia Polytechnic Institute, 1997.
[26] N. Hamilton, H. S. Kang, C. Meneveau, and R. B. Cal, Statistical analysis of kinetic energy entrainment in a model wind turbine array boundary layer, J. Renew. Sustain. Energy **4**, 063105 (2012).
[27] K. Viestenz and R. B. Cal, Streamwise evolution of statistical events in a model wind-turbine array, Bound.-Lay. Meteorol. **158**, 209 (2016).
[28] L. E. M. Lignarolo, D. Ragni, F. Scarano, C. J. Simão Ferreira, and G. J. W. van Bussel, Tip-vortex instability and turbulent mixing in wind-turbine wakes, J. Fluid Mech. **781**, 467 (2015).
[29] N. Hamilton and R. B. Cal, Anisotropy of the Reynolds stress tensor in the wakes of wind turbine arrays in Cartesian arrangements with counter-rotating rotors, Phys. Fluids **27**, 015102 (2015).
[30] T. Burton, N. Jenkins, D. Sharpe, and E. Bossanyi, *Wind Energy Handbook*, 2nd ed. (Wiley, New York, 2011).
[31] B. Wieneke, Stereo-PIV using self-calibration on particle images, Exp. Fluids **39**, 267 (2005).
[32] W. K. George, Jr., P. D. Beuther, and J. L. Lumley, *Proceedings of the Dynamic Flow Conference on Dynamic Measurements in Unsteady Flows* (Springer, Berlin, 1978), pp. 757–800.
[33] L. P. Chamorro and F. Porté-Agel, Turbulent flow inside and above a wind farm: A wind-tunnel study, Energies **4**, 1916 (2011).

[34] R. A. G. Tejada, Effects on support structure design due to wake-generated turbulence, M.S. thesis, Delft University of Technology, 2014.

[35] J. Annoni, P. Seiler, K. Johnson, P. Fleming, and P. Gebraad, *American Control Conference* (IEEE, Piscataway, 2014), pp. 2517–2523.

[36] P. Fleming, A. Ning, P. Gebraad, and K. Dykes, Wind plant system engineering through optimization of layout and yaw control, Wind Energy **19**, 329 (2016).

[37] M. J. Churchfield, S. Lee, J. Michalakes, and P. J. Moriarty, A numerical study of the effects of atmospheric and wake turbulence on wind turbine dynamics, J. Turbul. **13**, N14 (2012).

[38] R. J. Barthelmie, S. T. Frandsen, M. N. Nielsen, S. C. Pryor, P.-E. Rethore, and H. E. Jørgensen, Modelling and measurements of power losses and turbulence intensity in wind turbine wakes at Middelgrunden offshore wind farm, Wind Energy **10**, 517 (2007).